nature synthesis

Article

https://doi.org/10.1038/s44160-026-01104-6

Electrified direct epoxidation of light hydrocarbons using alkene-binding atomic sites

Received: 29 September 2025

Accepted: 26 May 2026

Published online: 25 June 2026

Check for updates

Yongxiang Liang[1,2,4], Yiqing Chen[1,2,4], Yu Yang[3], Rong Xia[1,2], Jianan Erick Huang[1,2], Zedong Zhang[1,2], Bosi Peng[1,2], Zeyan Liu[1,2], Huajie Ze[1,2], Aamir Hassan Shah[1,2], Yali Ji[1,2], Fengwang Li[3], Ke Xie[1,2] ✉ & Edward H. Sargent[1,2] ✉

Direct electrochemical epoxidation of alkenes could reduce the carbon intensity of epoxidation processes. However, highly selective electrified epoxidation is hindered by the competing oxygen evolution reaction. Analysis of the best-performing electrocatalysts reported to date reveals that propylene binds weakly to their surfaces while oxygen evolution intermediates predominate. Here we attempted to find catalysts on which surface-adsorbed propylene resides in proximity to reactive oxygen species. Screening a series of dopants revealed a volcano-type relationship between epoxidation activity and propylene adsorption, with indium-doped platinum–palladium oxide (In-PtPdOx) achieving the highest performance. The propylene oxide Faradaic efficiency reached 66% at 70 mA cm^{-2} and 58% at 100 mA cm^{-2}, with a high productivity of 1,080 μmol cm^{-2} h^{-1}. Integration into a membrane electrode assembly enabled a 46 wt% propylene oxide stream. Mechanistic characterization indicated that indium incorporation elevates the valence of platinum, strengthening metal–π C–C interactions with propylene and balancing propylene co-adsorption with reactive oxygen intermediates, thereby suppressing the oxygen evolution reaction and enabling highly selective epoxidation.

Propylene oxide (PO) is a precursor to plastics such as polyurethanes[1–3]. Global demand reached 10 million tonnes per annum in 2024 and is projected to rise to 18 million tonnes per annum by 2035 (ref. 4). Industrial PO is currently produced by halohydrin[5–8] and hydrogen peroxide oxidation routes[9–12], both of which rely on hazardous reagents and energy-intensive conditions, contributing to a carbon intensity of 3–4 tonne carbon dioxide equivalent (CO_2e) per tonne PO (refs. 13–15).

The electrochemical propylene epoxidation reaction (ePER) uses electricity and water as feedstocks; however, to date, reported productivities remain below 50 mA cm^{-2} (refs. 16–24). Reactive oxygen species are key intermediates in the electrooxidation process, and increasing the activity of oxygen species has been recognized as an efficient route to improve the electrooxidation performance[25–27]. As the onset of ePER occurs at a lower potential than the oxygen evolution reaction (OER), oxygen species can preferentially react with alkene molecules (Fig. 1a). At the higher potentials needed to achieve higher current densities, however, these reactive oxygen intermediates increasingly drive the competing OER, which lowers the Faradaic

[1]Department of Chemistry, Northwestern University, Evanston, IL, USA. [2]Department of Electrical and Computer Engineering, Northwestern University, Evanston, IL, USA. [3]School of Chemical and Biomolecular Engineering and ARC Centre of Excellence for Green Electrochemical Transformation of Carbon Dioxide, The University of Sydney, Sydney, New South Wales, Australia. [4]These authors contributed equally: Yongxiang Liang, Yiqing Chen. ✉e-mail: ke-xie@northwestern.edu; ted.sargent@northwestern.edu

https://doi.org/10.1038/s44160-026-01104-6

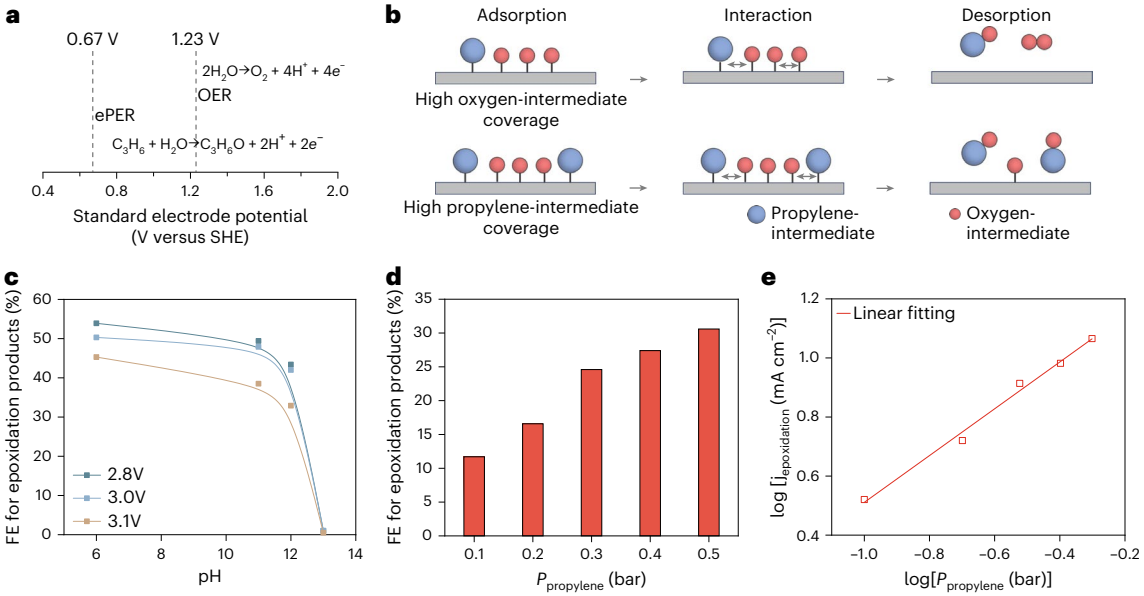

Fig. 1 | Chemical picture of electrochemical propylene epoxidation reaction (ePER) and routes to increasing its selectivity at high current densities. **a**, The standard electrode potentials of OER and ePER (versus standard hydrogen electrode (SHE)). **b**, Propylene epoxidation at high oxygen-intermediate versus high propylene-intermediate coverage. The blue and red circles represent propylene intermediates and oxygen intermediates, respectively. **c**, The impact of pH on FE to epoxidation products over the platinum–palladium oxide (PtPdOx) catalyst. The measured potential was converted to the reversible hydrogen electrode (RHE) scale without ohmic compensation. **d**, The impact of propylene partial pressure on FE for epoxidation products over the PtPdOx catalyst at a propylene partial pressure ranging from 0.1 to 0.5 bar. The total pressure was balanced by nitrogen. **e**, The linear fitting of the log of the partial current density of epoxidation products against the log of propylene partial pressure. The linear regression yielded a coefficient of determination (R^2) value of 0.99, indicating a strong correlation.

efficiency (FE) towards ePER (refs. 18,28). Thus, enhancing the activity or abundance of oxygen intermediates alone does not address the need for high selectivity at high productivity[29–32].

In the Langmuir–Hinshelwood (L–H) mechanism for the electrooxidation process[33,34], oxygen intermediates and propylene intermediates are co-adsorbed on the catalyst surface before reacting to form epoxidation products. We hypothesized that catalyst design could be used to increase propylene adsorption (Fig. 1b).

Results and discussion

Electrochemical picture of propylene epoxidation

We began by studying the reaction mechanism on a baseline catalyst and for this we selected the best-performing ePER catalyst reported previously[20], platinum–palladium alloy oxide (PtPdOx; Methods). The onset potential for propylene oxidation was lower than that of the OER, consistent with the standard electrode potentials of both reactions (Supplementary Fig. 1). We sought to characterize how ePER selectivity depends on the availability of both oxygen species and propylene. We employed a flow cell and quantified epoxidation products using ^{1}H NMR (Supplementary Fig. 2). As the pH is increased from 6 to 12, the FE for total epoxidation products decreases progressively, then drops abruptly to zero at pH 13 (Fig. 1c). Thus, OH^- in the electrolyte increases coverage by O intermediates, which are necessary for ePER, but at the highest pH the surface becomes dominated by OER intermediates[35,36]. We varied the propylene partial pressure, finding that total epoxidation FE decreased from 36% at 0.5 bar to 12% at 0.1 bar (Fig. 1d). The slope of log (partial current density of epoxidation products) versus log (propylene partial pressure) is approximately 0.8, indicating a strong dependence on propylene coverage. By mixing strong adsorbate carbon monoxide with propylene, we found a substantial decrease in epoxidation FE and reaction rate, which further revealed propylene adsorption on the catalyst surface during the epoxidation process (Supplementary Fig. 3). These observations are collectively consistent with the L–H mechanism as the dominant reaction pathway, suggesting that optimizing propylene adsorption could improve ePER selectivity at high current densities.

Catalyst screening and material characterization

We investigated whether doping could tune propylene adsorption on PtPdOx (refs. 37,38). Eight candidate dopants at 1% atomic ratio were screened by evaluating epoxidation performance at a current density of 50 mA cm^{-2} (Supplementary Figs. 4 and 5). The propylene stripping potential was measured as a proxy for propylene adsorption strength (Supplementary Fig. 6). We found an empirical volcano relationship (Fig. 2a) between epoxidation rate and stripping potential, indicating that a moderate propylene adsorption leads to the best ePER selectivity. Indium (In) sits at the peak of the volcano plot.

We then characterized the composition, structure and chemical state of In-doped PtPdOx. Alloy nanoparticles on nitrogen-doped carbon (NC) were observed to aggregate into irregularly shaped nanoparticles upon annealing (Supplementary Figs. 7–9); indium doping does not appreciably alter morphology compared with undoped controls (Supplementary Fig. 10). The spatial distributions of Pt, Pd and In are uniform in energy dispersive X-ray spectroscopy (EDS) maps (Supplementary Fig. 11). X-ray diffraction (XRD) reveals both metallic Pt and tetragonal PdO with enhanced crystallinity compared to the undoped PtPd alloy (Fig. 2b and Supplementary Fig. 12). High-resolution transmission electron microscopy (HRTEM) reveals lattice fringes with a *d*-spacing of 0.21 nm and 0.27 nm corresponding to the Pt(111) and PdO(101) planes in the bulk phase, respectively (Fig. 2c). In 3*d* X-ray photoelectron spectroscopy (XPS) confirms that indium is in the +3 oxidation state (Supplementary Fig. 13). The Pd 3*d* binding energy at 337.0 eV, assigned to Pd^{2+}, changes little upon indium doping (Fig. 2d). The Pt $4f_{7/2}$ spectra display two components at 71.4 eV (Pt^0) and 73.3 eV (Pt^{2+}). The Pt^{2+} peak shifts to higher binding energy by 0.7 eV and 1.2 eV for 1 and 3% indium doping, respectively (Fig. 2e). The Pt L_3-edge X-ray absorption near edge structure (XANES) white-line peak (Supplementary Fig. 14) indicates that Pt is

https://doi.org/10.1038/s44160-026-01104-6

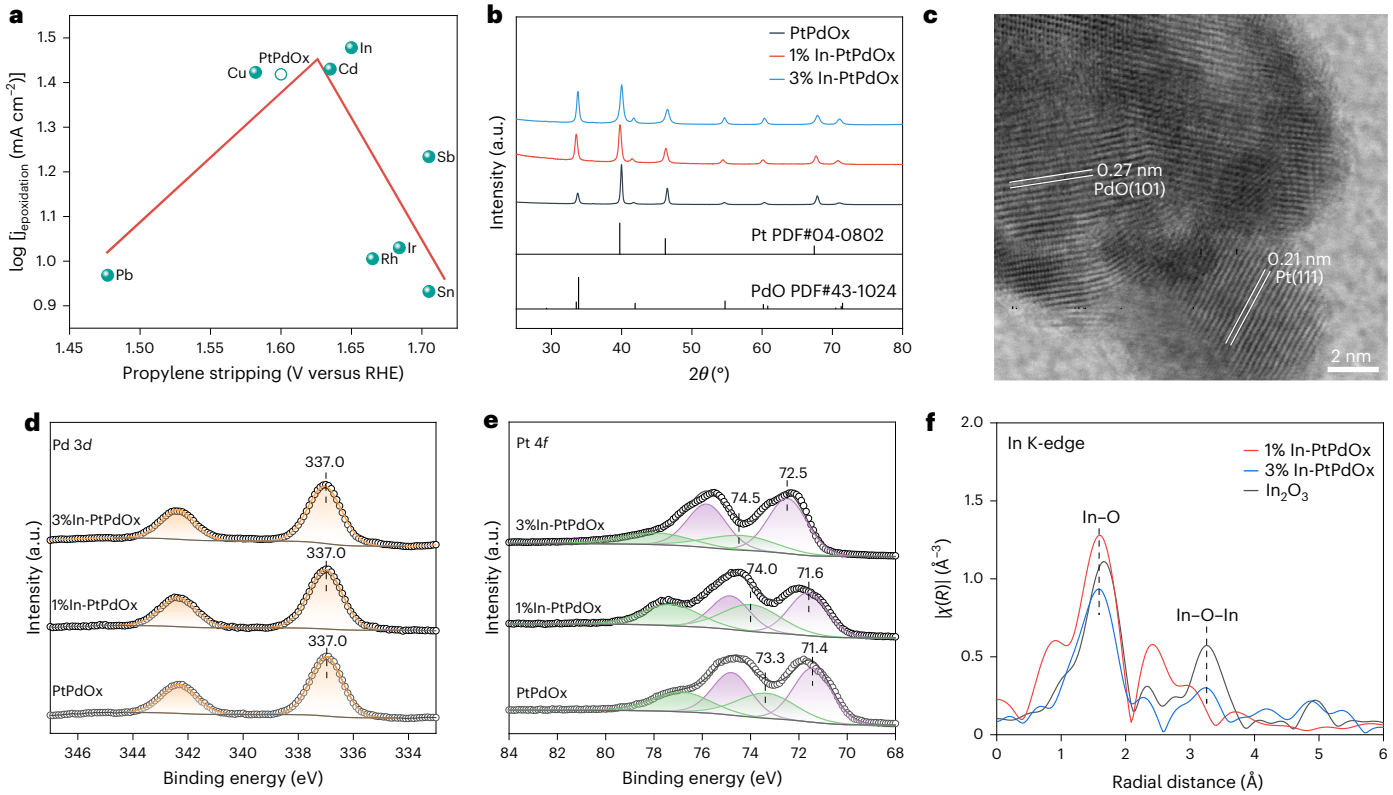

Fig. 2 | Catalyst screening and material characterization. a, Experimental relationship between propylene epoxidation rate and propylene stripping potential over pristine platinum–palladium oxide (PtPdOx, empty circle) and lead (Pb)-, copper (Cu)-, cadmium (Cd)-, indium (In)-, rhodium (Rh)-, iridium (Ir)-, antimony (Sb)- and tin (Sn)-doped PtPdOx (filled circles). **b**, X-ray diffraction (XRD) patterns of PtPdOx, 1%In-PtPdOx and 3%In-PtPdOx catalysts. The patterns of Pt (PDF#04-0802) and PdO (PDF#43-1024) were used as the reference. a.u., arbitrary units. **c**, High-resolution transmission electron microscopy (HRTEM) image of 1%In-PtPdOx. **d**, High-resolution Pd 3*d* X-ray photoelectron spectroscopy (XPS) spectra of PtPdOx, 1%In-PtPdOx and 3%In-PtPdOx catalysts. **e**, High-resolution Pt 4*f* XPS spectra of PtPdOx, 1%In-PtPdOx and 3%In-PtPdOx catalysts. The green and purple peaks correspond to the deconvoluted Pt^{2+} and Pt^{0} components, respectively. **f**, In K-edge extended X-ray absorption fine structure (EXAFS) spectra of 1%In-PtPdOx and 3%In-PtPdOx. The In K-edge spectrum of indium oxide (In_2O_3) was used as the reference.

in an average oxidation state between 0 and 2, with indium doping increasing the oxidation state, consistent with XPS. X-ray absorption fine structure (EXAFS) shows that indium does not materially alter the Pd and Pt coordination environments. In K-edge EXAFS shows an In–O bond at a radial distance of approximately 1.6 Å (Fig. 2f); with EXAFS fitting yielding an In–O coordination number of approximately 4.9 (Supplementary Fig. 15 and Table 1). We see no appreciable In–O–In coordination at approximately 3.3 Å, characteristic of In_2O_3 clusters, in the 1% doped sample. Taken together, these results indicate that indium is largely atomically dispersed in the 1% In-doped samples. Studies of 3% indium doping, including the emergence of In–O–In coordination, suggest that these more heavily doped samples form In_2O_3 clusters.

In summary, indium doping increases the oxidation state of Pt within the surface metal-oxide matrix while changing the Pd valence state only slightly. Pt sites with higher oxidation state are expected to exhibit stronger electrophilicity, potentially enhancing the adsorption of nucleophilic propylene.

Evaluation of propylene epoxidation performance

Previous studies have emphasized high epoxidation FE, yet achieving product concentrations suitable for cost-effective separation remains unexplored. By constructing zero-gap membrane electrode assembly (MEA) devices, we further optimized the product distribution in the anode gas stream and electrolyte (Fig. 3a and Supplementary Fig. 16). PO crossover from anode gas stream to electrolyte decreased from 83% in the flow cell with unbuffered electrolyte to 29% in the MEA. Consequently, the PO selectivity among total epoxidation products rose from 18% in the flow cell to 98% in the MEA (Fig. 3b). This shift towards PO-dominant products substantially reduces estimated separation costs relative to propylene glycol (PG), which is beneficial to technoeconomic analysis (Supplementary Fig. 17).

We then optimized electrocatalytic performance in the MEA, focusing on current densities of 60–100 mA cm^{-2}, above the 10–50 mA cm^{-2} range of previous reports. The FE declines from 50 to 36% as current density increases from 60 to 100 mA cm^{-2} over pristine PtPdOx (Fig. 3c). Systematic variation of indium doping (0, 0.5, 1, 1.5, 2 and 3% atomic ratio) showed that PO FE increases with indium content, reaching a maximum over 1%In-PtPdOx; further increases in indium doping level led to a gradual decline in PO FE (Supplementary Figs. 18–20). For 1% In-doped PtPdOx, the PO FE peaks at 66% at 70 mA cm^{-2} and remains at 58% at 100 mA cm^{-2}. Correspondingly, OER is diminished in the optimally In-doped sample (Supplementary Fig. 21). The PO production rate reaches 1,080 μmol cm^{-2} h^{-1} for 1%In-PtPdOx, 1.6 times that of pristine PtPdOx (Fig. 3d), indicating that indium doping enhances intrinsic epoxidation activity. The reduced efficiency of the 3% In sample results from the formation of aggregated In_2O_3 clusters, which do not effectively increase propylene adsorption in proximity to oxygen-supplying catalytic sites.

We then investigated the capacity of the optimized MEA system to reduce PO crossover to the cathode, thereby increasing PO concentration on the anode side. Similar liquid product profiles over PtPdOx and In-doped PtPdOx indicated that PO crossover is dominated by membrane-mediated mass transport rather than ionic migration

https://doi.org/10.1038/s44160-026-01104-6

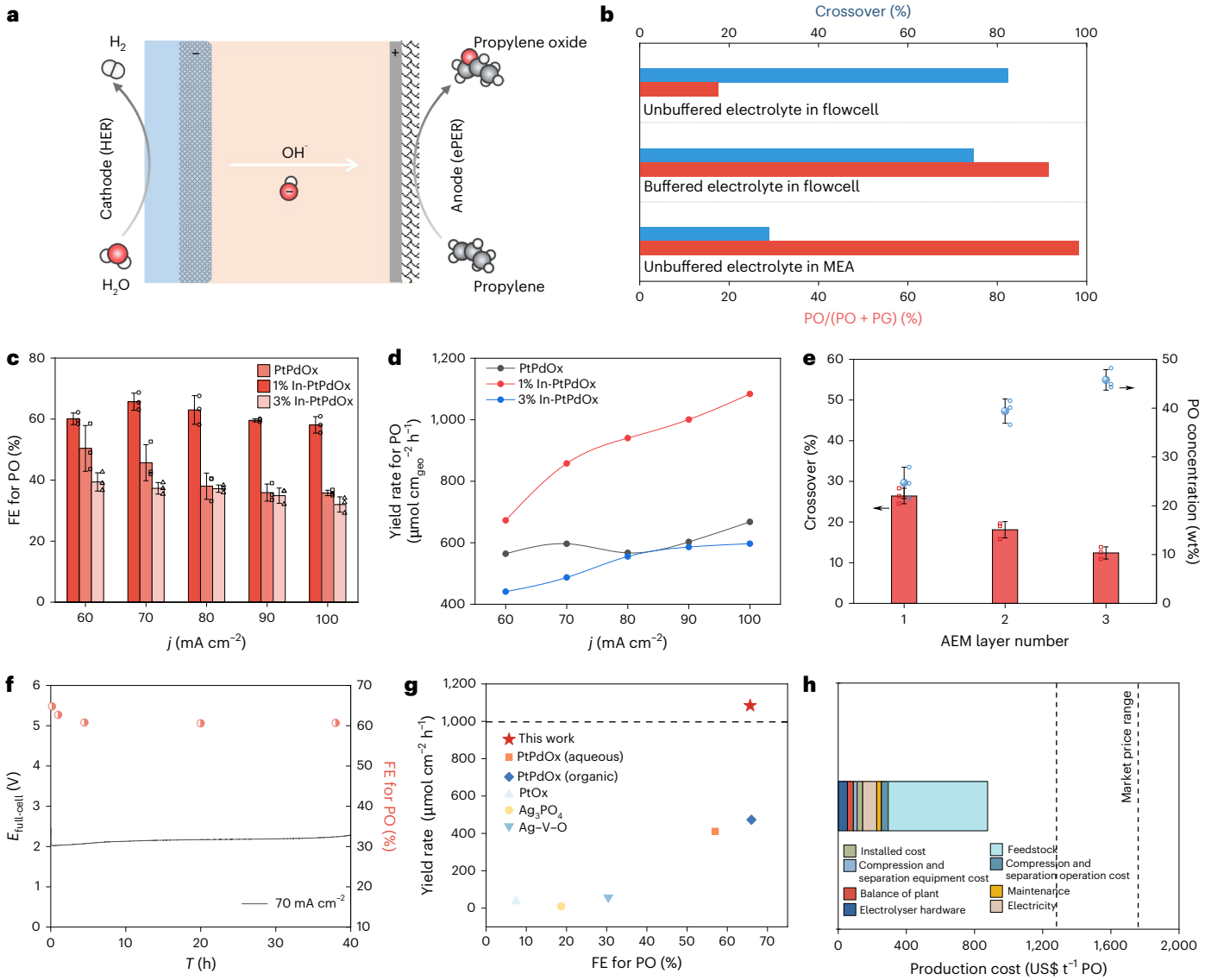

Fig. 3 | Propylene epoxidation membrane electrode assembly (MEA) system performance. a, Electrochemical propylene epoxidation reaction (ePER) paired with the hydrogen evolution reaction (HER) in a membrane electrode assembly system. **b**, Propylene oxide (PO) product ratio in total epoxidation products (PO + propylene glycol (PG)) and corresponding crossover ratio in flow cell with a non-buffer electrolyte, flow cell with a buffer electrolyte and membrane electrode assembly with a non-buffer electrolyte, respectively. **c**, Total Faradaic efficiency (FE) for PO at current densities ranging from 60 to 100 mA cm^{-2} over the platinum–palladium oxide (PtPdOx), 1%In-PtPdOx and 3%In-PtPdOx catalysts. **d**, The yield rate for PO at a current ranging from 60 to 100 mA cm^{-2} over PtPdOx, 1%In-PtPdOx and 3%In-PtPdOx. **e**, Crossover and corresponding PO concentration in the anode outlet stream of MEA with different anion exchange membrane layers. **f**, Stability test of ePER at 70 mA cm^{-2} in MEA. **g**, Summary of ePER performance over 1%In-PtPdOx in FE and yield rate for PO compared with the state-of-the-art catalysts. **h**, Cost breakdown for PO electrosynthesis using 1%In-PtPdOx in MEA. The error bars in **c** and **e** represent the standard deviation (s.d.) of three independent experiments ($n = 3$) and the corresponding data distribution is represented by hollow points. Data are presented as mean ± s.d.

or water crossover (Supplementary Fig. 22). To reduce membrane-mediated mass transport, anion exchange membrane (AEM) layers were added to increase the product diffusion distance, lowering crossover to 12% while increasing anode-side product concentration to 46 wt% (Fig. 3e and Supplementary Fig. 23). Stable operation was maintained for 40 hours with a PO FE of 60% at 70 mA cm^{-2}, benefited by mitigation of electrode flooding (Fig. 3f). Post-test characterization showed no notable morphological changes to the 1%In-PtPdOx catalyst (Supplementary Fig. 24). These performance metrics compare favourably with those of previously reported ePER systems (Fig. 3g and Supplementary Table 5). Technoeconomic analysis estimates a PO production cost of approximately US$900 tonne $(t)^{-1}$. This is encouraging compared with the current market price of US$1,300–1,800 t^{-1} (Fig. 3h, Supplementary Fig. 25 and Supplementary Note 1)[39].

Mechanism of electrochemical propylene epoxidation reaction

We sought to further study the surface intermediates associated with oxygen and propylene adsorption. To probe oxygen intermediate adsorption, linear sweep voltammetry (LSV) in an N_2 atmosphere was used to compare OER activity between PtPdOx, 1%In-PtPdOx and 3%In-PtPdOx: once normalized by electrochemical surface area (ECSA), all three catalysts show similar OER activity (Fig. 4a and Supplementary Fig. 26). Operando surface-enhanced Raman spectroscopy (SERS) (Supplementary Fig. 27) shows a sharp peak at 933 cm^{-1} assigned to ClO_4^- from the electrolyte (Fig. 4b)[40]. The bands at 508 cm^{-1} and 577 cm^{-1} are assigned to the stretching vibration of adsorbed Pd–OH (ref. 22) and Pt–OH (refs. 41,42), respectively, while the feature near 821 cm^{-1} corresponds to adsorbed peroxide species (*O–O) on the catalyst surface[43]. The Pd–OH, Pt–OH and *O–O band positions are

https://doi.org/10.1038/s44160-026-01104-6

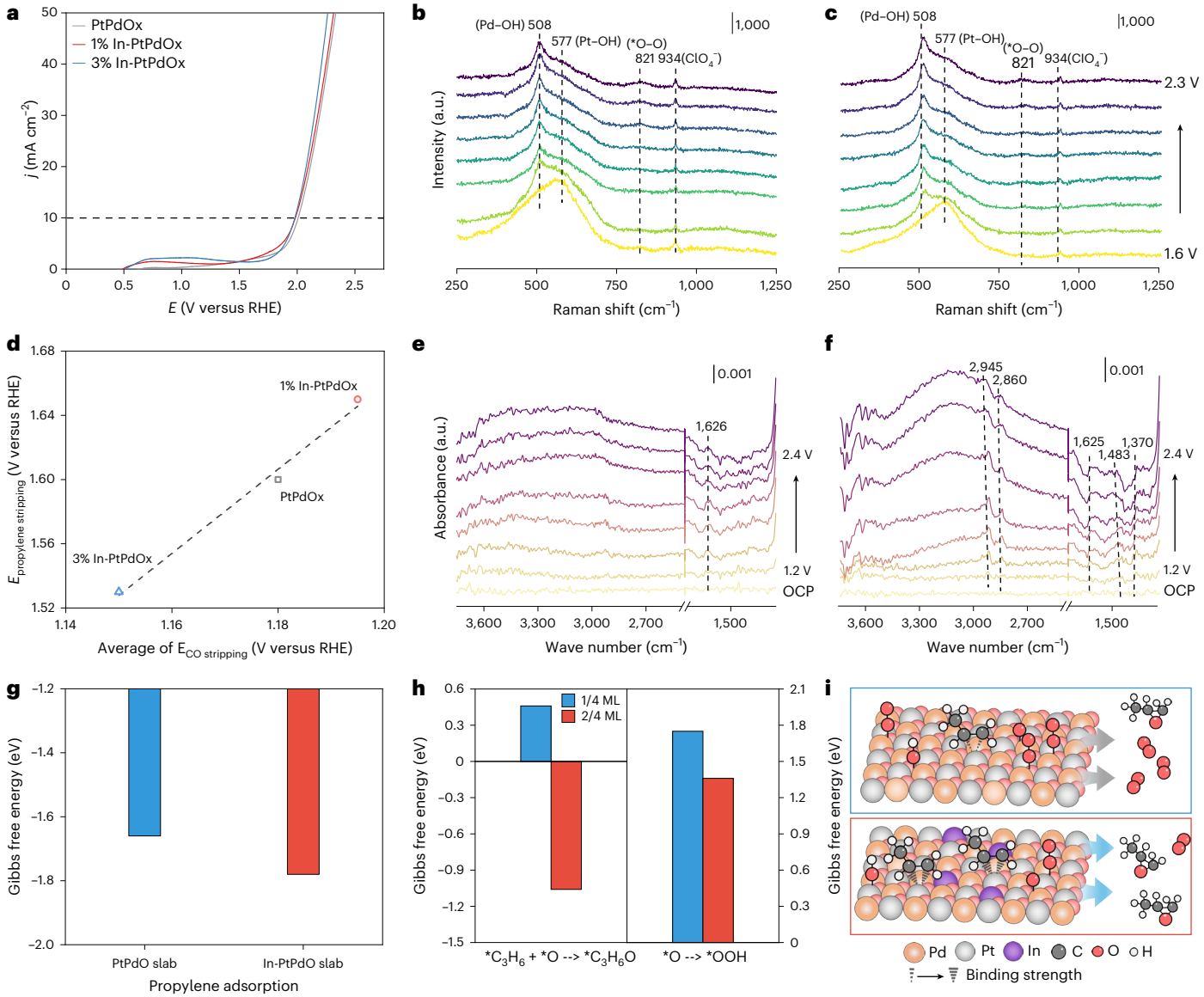

Fig. 4 | Mechanistic study of electrochemical propylene epoxidation reaction (ePER) in In-doped platinum–palladium oxide (PtPdOx) catalysts. a, Linear sweep voltammetry (LSV) polarization curves of PtPdOx, 1%In-PtPdOx and 3%In-PtPdOx catalysts under nitrogen (N_2) atmosphere. **b**,**c**, Operando electrochemical surface-enhanced Raman spectroscopy (SERS) of electro-oxidized Au@PtPdOx (**b**) and Au@1%In-PtPdOx (**c**) at the applied potential ranging from 1.6 to 2.3 V (versus the reversible hydrogen electrode (RHE)) in N_2-saturated 0.5 M sodium perchlorate ($NaClO_4$) electrolyte. a.u., arbitrary units. **d**, Linear fitting of propylene stripping potential and carbon monoxide (CO) stripping average potential. The linear regression yielded a coefficient of determination (R^2) value of 0.99, indicating a strong correlation. **e**,**f**, Operando attenuated total reflectance-surface enhanced infrared absorption spectroscopy (ATR-SEIRAS) spectra of 1%In-PtPdOx catalysts at the applied potential range from 1.2 to 2.4 V (versus RHE) in N_2-saturated (**e**) and propylene-saturated (**f**) 0.5 M $NaClO_4$ electrolyte. The spectra collected at the open-circuit potential (OCP) served as baseline. **g**, Gibbs free energy of propylene adsorption on PtPdO and In-PtPdO slabs, respectively. **h**, Gibbs free energy differences of $*C_3H_6$-to-$*C_3H_6O$ pathway and *O-to-*OOH pathway under 1/4 monolayer (ML) and 2/4 ML of propylene coverage. **i**, Schematic illustration of reaction process on PtPdO (top) and In-PtPdO (bottom) slab by tuning the coverage of $*C_3H_6$ and O intermediates, respectively.

little affected by indium doping (Fig. 4c and Supplementary Fig. 28), indicating that oxygen intermediate adsorption strength is not notably modified by indium doping, consistent with the LSV results. The Pt–OH to Pd–OH intensity ratio of 1%In-PtPdOx is lower than that of PtPdOx and 3%In-PtPdOx. By contrast, the $*O–O/ClO_4^-$ ratio is higher for 3% indium doped catalysts, indicating an increased surface coverage of *O–O intermediates. To summarize, 1% indium doping reduces Pt–OH formation, freeing more active sites for propylene adsorption. Excessive indium doping promotes oxygen-related species, accounting for the performance decline observed for 3%In-PtPdOx.

To elucidate the adsorption mode of propylene on the catalyst surface, we used carbon monoxide (CO) as a probe molecule and conducted CO stripping voltammetry (Supplementary Fig. 29). CO is known to bind to metal active sites via metal–carbon bonds, providing a benchmark for comparing adsorption energetics[44,45]. We identified a strong linear relationship between CO stripping potentials and the corresponding propylene oxidation potentials (Fig. 4d and Supplementary Fig. 30). This indicates that propylene oxidation occurs on sites with similar binding characteristics to CO, implying that propylene is likewise anchored to the catalyst surface through metal–carbon interactions during the oxidation process. Operando attenuated total reflectance-surface enhanced infrared absorption spectroscopy (ATR-SEIRAS) was used to probe propylene adsorption structure and strength across the catalyst series (Supplementary Fig. 31). In

N_2-saturated electrolyte, only the band associated with adsorbed OH bending at 1,626 cm^{-1} is observed (Fig. 4e). Upon introduction of propylene, methyl C–H (2,950–2,800 cm^{-1}) and in-phase CH_2 (1,386 and 1,370 cm^{-1}) vibrations appear, indicating surface-bound propylene (Fig. 4f and Supplementary Fig. 32). The C=C stretching band appears at 1,521 cm^{-1} for undoped samples and at 1,483 cm^{-1} for doped samples. This is consistent with indium doping strengthening metal–π C–C interactions and weakening the C=C double bond in propylene[28,46] and accounts for the redshift in vibrational frequency. This redshift, together with a shift in Stark effect under increasing anodic potential, supports chemical adsorption of propylene ($*C_3H_6$) via π bonding. Replacing propylene with the less nucleophilic ethylene consistently reduced the epoxidation FE (Supplementary Fig. 33), further supporting the strategy that tuning alkene adsorption strength is key to controlling electrochemical alkene epoxidation selectivity.

To enable comparison with experimental results, we conducted density functional theory (DFT) calculations, examining the effect of indium doping on propylene epoxidation (Supplementary Figs. 34 and 35). The indium substitution of the Pd site in the In-PtPdO slab is energetically favourable as the stable configuration (Supplementary Fig. 36). The optimized geometry shows $*C_3H_6$ binding via the C=C bond on Pt while *O occupies a neighbouring Pd/Pt site (Supplementary Fig. 37). The calculated Gibbs free energy of propylene adsorption on the In-PtPdO slab is −1.78 eV, which is 0.12 eV more negative (and therefore more favourable) than on the pristine PtPdO slab (Fig. 4g). Varying propylene coverage from 1/4 monolayer (ML) to 2/4 ML (Fig. 4h and Supplementary Fig. 38), *O serves as the branching point between epoxidation and OER. Increasing propylene surface coverage lowers the activation barrier for propylene oxidation by 1.52 eV, whereas the barrier for the oxygen evolution pathway decreases by 0.39 eV (Supplementary Fig. 39). Thus, higher propylene coverage favours epoxidation over OER (Fig. 4i).

Conclusion

In summary, electrified propylene epoxidation performance is enhanced over 1%In-PtPdOx, reaching a PO FE of 66% at 70 mA cm^{-2} and producing a concentrated PO stream with 46 wt% purity. A PO yield rate of 1,080 µmol cm^{-2} h^{-1} was achieved at 100 mA cm^{-2}. Indium doping increases hydrocarbon adsorption through metal–π C–C interactions, enabling selective epoxidation to outcompete the parasitic oxygen evolution reaction. Both experimental spectroscopy and DFT calculations are consistent with a Langmuir–Hinshelwood (L–H) mechanism for ePER, where both $*C_3H_6$ and reactive oxygen intermediates are co-adsorbed on the catalyst surface. Doping enhances propylene adsorption by increasing the electrophilicity of active sites, and balanced co-adsorption of $*C_3H_6$ and reactive oxygen intermediates favours ePER over OER.

Methods

Chemicals and materials

All chemicals were used as received without further purification. Sodium tetrachloropalladate(II) (Na_2PdCl_4, 98%), palladium(II) chloride ($PdCl_2$, 99.9%), chloroplatinic acid hexahydrate ($H_2PtCl_6{\cdot}6H_2O$, ACS reagent), indium(III) chloride ($InCl_3$, 99.999%), ethylene glycol (EG), urea, deuterium oxide (D_2O, 99.99 atom% D), sodium perchlorate ($NaClO_4$, ≥98.0%), sodium phosphate (Na_3PO_4, 96%), phosphoric acid (H_3PO_4, 85 wt% in H_2O), gold(III) chloride trihydrate ($HAuCl_4{\cdot}3H_2O$, 99%), sodium citrate dihydrate (≥99%), hydrochloric acid (HCl, 37%) and ascorbic acid (AA) were purchased from Sigma Aldrich. Toray carbon paper 120 (wet proofed) and Vulcan XC-72R carbon black were obtained from Fuel Cell Store. The anion exchange membrane (AEM, Sustainion X37-50 grade 60) was purchased from Dioxide Materials. Nafion 115 proton exchange membrane and Nafion D520CS (5 wt%) were purchased from Ion Power. Ultra-pure water (resistivity: 18.2 MΩ cm^{-1} at 25 °C) was used throughout the experiments.

Synthesis of NC support

The NC support was prepared by nitriding carbon black following a previously reported method with minor modification[47]. Vulcan XC-72R carbon black (0.083 mol, 1 g) and urea (0.025 mol, 1.5 g) were thoroughly mixed and ground. The mixture was sealed in a porcelain boat with aluminium foil and calcined at 150 °C for 2 h (heating rate: 2 °C min^{-1}) and then at 300 °C for 4 h (heating rate: 5 °C min^{-1}). The resulting powder was washed with water and ethanol to remove unreacted urea and dried at 60 °C for further use.

Synthesis of In-doped PtPd on NC support

Indium-doped PtPd catalysts were synthesized using a wet-chemical reduction method. NC (9.17 mmol, 110 mg) was dispersed in EG (200 ml). Precursor solutions of Na_2PdCl_4 (0.25 mmol, 73.55 mg in 5 ml EG), $H_2PtCl_6{\cdot}6H_2O$ (0.25 mmol, 129.48 mg in 5 ml EG) and $InCl_3$ (0.025 mmol, 5.53 mg in 5 ml EG) were prepared. The Pd and Pt solutions were added dropwise to the NC dispersion under vigorous stirring. The indium doping level was controlled by adjusting the volume of $InCl_3$ solution. The mixture was stirred for 30 min, ultrasonicated for 1 h and then reduced with $NaBH_4$ (9.52 mmol, 360 mg in 60 ml EG) added at 1 ml min^{-1}. The resulting suspension was washed with acetone, centrifuged and dried to obtain the catalyst. PtPd, 1%In-doped PtPd and 3%In-doped PtPd catalysts were prepared by adding 0, 1 and 3 ml $InCl_3$ solution, respectively. All screened catalysts were prepared by the same method, except for substituting $InCl_3$ with the corresponding metal chloride.

Preparation of In-PtPdOx anode electrodes

The catalyst ink was prepared by dispersing 40 mg of In-PtPd on NC in a mixed solvent of water (0.5 ml) and ethanol (5.5 ml), followed by ultrasonication for 30 min. Then 160 µl Nafion solution was added and the mixture was ultrasonicated for another 1 h. The ink was airbrushed onto Toray-120 carbon paper (3 × 3 cm^2) and dried, resulting in a catalyst loading of 2 mg cm^{-2}. The prepared electrode was annealed at 500 °C for 3 h (heating rate: 3 °C min^{-1}). The electrode was cooled to room temperature, and 200 µl of 2 wt% Nafion was drop-cast onto the surface with catalysts to form the anode electrodes, which were labelled PtPdOx, 1%In-PtPdOx and 3%In-PtPdOx, respectively.

Electrochemical experiments

The ePER experiments were conducted in an MEA electrolyser. The MEA consisted of a 1.5 × 1.5 cm^2 anode electrode, a 2.5 × 2.5 cm^2 ion exchange membrane and a 1 × 1 cm^2 platinized titanium fibre felt cathode from Fuel Cell Store. The electrolyser was sealed with a 0.02-inch-thick insulated gasket to prevent electrolyte leakage. The reaction area was regulated by a 1 × 1 cm^2 hole in the gasket. A constant flow of 0.5 M $NaClO_4$ was supplied to the cathode as the electrolyte, while propylene gas (20 sccm) was fed to the anode. Current densities were applied incrementally from 60 to 100 mA cm^{-2} using a Biologic SP-300 potentiostat. The same experimental procedure was applied to ethylene oxidation, with ethylene substituted for propylene.

The flow cell used in ePER experiments was configured with a three-electrode setup. The prepared anode electrode, Ag/AgCl reference electrode (containing 1 M KCl electrolyte) and Ni foam were employed as the working, reference and counter electrodes, respectively. The pre-activated Nafion 115 proton exchange membrane was used to separate the anode and cathode chambers. Either 1 M $NaClO_4$ or 1 M $NaClO_4$ with 0.25 M Na_3PO_4 (buffer electrolyte, pH adjusted to 6 by adding H_3PO_4) was used as the electrolyte. The geometric reaction area was confined to 1 cm^2. A constant flow of electrolyte was cycled in the anode and cathode chambers, respectively. Propylene was flowed at a constant rate of 20 sccm. All potentials in this work were measured against a reference electrode (E versus Ag/AgCl), except those in MEA experiments that were converted to the reverse hydrogen electrode (RHE) scale by the following equation: E (versus RHE) = E (versus Ag/AgCl) + 0.222 V + 0.059 × pH.

Product analysis

Gas products (CO_2 and O_2) were quantified using offline gas chromatography (GC-2014, Shimadzu) with a flame ionization detector (FID) and a thermal conductivity detector (TCD). In the MEA, the liquid products from the anode channel were separated and collected using a cold trap. In one full cycle, the FE for liquid products was calculated by collecting and analysing products from both the anode and cathode channels during the same period. In the flow cell, the liquid products in the anodic liquid chamber and gas chamber were analysed separately and the liquid products in the gas chamber were also collected using the cold trap. The crossover in the flow cell and MEA is defined as the ratio of epoxides (PO, PG) in the electrolyte compared to the total epoxides. The PO selectivity in the MEA is defined as the fraction of PO within the total epoxidation products (PO and PG). Liquid products (PO, PG, acetate, acetic acid) were analysed using ^{1}H NMR spectroscopy (Bruker Avance III 600 MHz) using DMSO/D_2O as an internal standard. Typically, 0.5 ml of the liquid to be tested was mixed with 0.1 ml D_2O with DMSO as the internal standard. The area ratio of liquid product peaks to the DMSO peak was used to calculate the FE for liquid products based on known DMSO concentration.

Electrochemical measurements

First, 5 mg catalyst powder was dispersed in 1 ml of solvent (V_{H2O}:$V_{iso\text{-}proponal}$ = 1:1) by ultrasound for 30 min. Next, 20 µl Nafion solution was added to the above mixture with another 30 min of sonication to obtain the ink. Then, 5 µl of the ink with 3 mm diameter was dropped on the glassy carbon electrode. The glassy carbon electrode, Ag/AgCl electrode and Pt were used as the working, reference and counter electrodes, respectively. The cyclic voltammetry (CV) and linear scan voltammetry (LSV) curves were recorded at a scan rate of 100 mV s^{-1} in a single cell containing N_2-saturated 0.5 M $NaClO_4$ electrolyte. The electrochemical surface area (ECSA) was determined using double-layer capacitance (C_{dl}). The C_{dl} was obtained by measuring the capacitive current associated with double-layer charging. CV in the non-Faradaic potential range was recorded by changing the scan rate from 20 to 100 mV s^{-1}. By linear fitting the current difference in the middle of the potential window against the scan rate, the corresponding slope obtained is twice that of the C_{dl}.

The CO stripping experiments were conducted in a single cell. First, 0.5 M $NaClO_4$ was bubbled with high-purity N_2 for at least 15 min. The electrode was pretreated using a CV scan from 0 to 1.9 V (versus RHE) for 6 cycles to remove possible adsorption species. After that, a constant potential was applied at 0.2 V (versus RHE) while the gas was switched to CO for another 15 min, followed by N_2 purging for 15 min to remove the excess CO in the electrolyte. Two cyclic voltammograms were recorded from 0 to 1.7 V (versus RHE) at a scan rate of 100 mV s^{-1}. No electrochemical CO oxidation peak was observed in the second CV cycle, indicating the oxidation peak in the first cycle came from the adsorbed CO on the catalyst surface. Propylene stripping was conducted by changing CO to propylene and the propylene stripping CV was recorded from 0 to 1.9 V (versus RHE).

Characterization

The morphologies of the samples were recorded using high-resolution transmission electron microscopy (TEM) (BioCryo JEOL JEM-3200FS). Aberration corrected scanning transmission electron microscopy (STEM) images and energy-dispersive X-ray spectroscopy (EDS) mappings were taken using a JEOL ARM200CF TEM instrument equipped with a dual SDD EDS detector. X-ray diffraction (XRD) patterns were collected using a Rigaku SmartLab diffractometer equipped with a Cu Kα radiation source (λ = 1.5406 Å). X-Ray photoelectron spectroscopy (XPS) was carried out on a Thermo Scientific Nexsa G2 system equipped with a monochromatic Al Kα X-ray source. Depth profiling was performed using an EX06 monatomic and cluster Ar ion source. The binding energies were corrected for specimen charging by referencing C 1*s* to 284.8 eV. All X-ray absorption spectroscopy (XAS) spectra were collected at the Australian Synchrotron in Clayton, Victoria, Australia, using the high-flux 1.9 T wiggler XAS Beamline operating in slew scan mode. XAS spectra were collected in transmission mode on sample pellets prepared as a homogenous mixture of catalyst powder with cellulose as a binding and filling agent.

The operando Raman experiments were carried out on a Renishaw inVia Raman microscope equipped with a water immersion objective (×63) lens with a 633 nm laser. To obtain the structural evolution of electrocatalysts with the change in electrode potential, we applied surface-enhanced Raman spectroscopy (SERS) by coating catalysts on the Au nanoparticles (NPs). Au NPs were prepared according to a previous report[48]. Typically, 2.424 ml of 1 wt% $HAuCl_4{\cdot}H_2O$ solution was added to 200 ml of deionized water. The above solution was heated to boiling in an oil bath, and then 1.5 ml of 1 wt% sodium citrate solution was quickly injected under vigorous stirring. The heating and stirring should be maintained for at least 30 min after the colour of the solution changes from light yellow to brick red. The Au colloid was cooled to room temperature and stored in the dark for further use. To prepare the Au@PtPd NPs, $PdCl_2$ was dissolved in 10 mM HCl to prepare 1 mM of Pd precursor. Then, 200 µl of 1 mM H_2PtCl_6 and 200 µl of Pd precursor were added to 10 ml of Au colloid. The mixture was vigorously stirred for 10 min at room temperature. Then, 400 µl of 10 mM AA was injected slowly for 10 min of reaction. The mixture was centrifuged and redispersed in water. Then, 5 µl of Au@PtPd colloid was dropped onto glassy carbon as the working electrode. The Au@1%In-PtPd NPs were synthesized by a similar method except for adding an additional 4 µl of 1 mM $InCl_3$ solution. The Au@PtPdOx and Au@1%In-PtPdOx were prepared by pre-oxidation of the corresponding alloy under positive potential during operando Raman measurements.

The operando attenuated total reflectance-surface enhanced infrared spectroscopy (ATR-SEIRAS) measurements were carried out on a Bruker Vertex 80 V spectrometer. A PIKE VeeMAX III variable angle ATR sampling accessory with a 10 ml Jackfish spectroelectrochemical cell was used as the electrochemical test system. First, 50 nm of Au was sputtered on a face-angled Si crystal (60°) and then the catalyst was drop-casted on the Au thin film. Propylene-saturated or N_2-saturated 0.5 M $NaClO_4$ was used as the electrolyte. All spectra were collected at a resolution of 4 cm^{-1}.

DFT calculations

All spin-polarized density functional theory (DFT) calculations were conducted using the Vienna Ab Initio Simulation Package (VASP)[49,50]. Electron–ion interactions were described by the projector-augmented wave (PAW) method[51] and the exchange–correlation effects were treated within the generalized gradient approximation (GGA) using the Perdew–Burke–Ernzerhof (PBE) functional[52,53]. Long-range van der Waals interactions were accounted for using Grimme's DFT-D3 correction with Becke–Johnson damping[54,55]. All calculations used a plane-wave energy cutoff of 450 eV. Structures were optimized until atomic forces were below 0.03 eV Å^{-1} and electronic self-consistency was achieved with a total energy convergence threshold of 10^{-4} eV. Solvation effects were considered using the implicit solvation model implemented in VASPsol++ (refs. 56,57).

Techno-economic analysis

Key operational parameters, including current density, cell voltage and Faradaic efficiency, were integrated into the model using experimental results obtained in this study (see Supplementary Table 2 for the reference scenario). The system was scaled to an industrial production capacity of 600,000 kg of propylene oxide per day, with a projected operational lifespan of 20 years. In the base case scenario, electricity costs were set at US$0.05 kWh^{-1} and the sensitivity analysis considered electricity prices ranging from US$0.03–0.07 kWh^{-1}. The downstream separation process was simulated using ASPEN Plus V14.0.

Comprehensive cost breakdowns and assumptions are provided in Supplementary Note 1.

Data availability

Source data are provided with this paper. All other data supporting the findings of this study are available within the Article and its Supplementary Information.

References

1. Herzberger, J. et al. Polymerization of ethylene oxide, propylene oxide, and other alkylene oxides: synthesis, novel polymer architectures, and bioconjugation. *Chem. Rev.* **116**, 2170–2243 (2016).
2. Khatib, S. J. & Oyama, S. T. Direct oxidation of propylene to propylene oxide with molecular oxygen: a review. *Catal. Rev.* **57**, 306–344 (2015).
3. Kube, P. et al. Green synthesis of propylene oxide directly from propane. *Nat. Commun.* **13**, 7504 (2022).
4. *Propylene Oxide (PO) Market Analysis: Industry Market Size, Plant Capacity, Production, Operating Efficiency, Demand & Supply, End-User Industries, Sales Channel, Regional Demand, Foreign Trade, Company Share, 2015-2036* https://www.chemanalyst.com/industry-report/propylene-oxide-po-market-755 (2025).
5. Chi, M. et al. Spatial decoupling of bromide-mediated process boosts propylene oxide electrosynthesis. *Nat. Commun.* **15**, 3646 (2024).
6. Leow, W. R. et al. Chloride-mediated selective electrosynthesis of ethylene and propylene oxides at high current density. *Science* **368**, 1228–1233 (2020).
7. Nijhuis, T. A., Makkee, M., Moulijn, J. A. & Weckhuysen, B. M. The production of propene oxide: catalytic processes and recent developments. *Ind. Eng. Chem. Res.* **45**, 3447–3459 (2006).
8. Wang, J. et al. Electrochemical epoxidation of propylene to propylene oxide via halogen-mediated systems. *ACS Omega* **8**, 46569–46576 (2023).
9. Fan, L. et al. Selective production of ethylene glycol at high rate via cascade catalysis. *Nat. Catal.* **6**, 585–595 (2023).
10. Ko, M. et al. Direct propylene epoxidation with oxygen using a photo-electro-heterogeneous catalytic system. *Nat. Catal.* **5**, 37–44 (2021).
11. Kwon, O., Zeynep Ayla, E., Potts, D. S. & Flaherty, D. W. Influence of Ti-incorporated zeolite topology and pore condensation on vapor phase propylene epoxidation kinetics with gaseous H_2O_2. *Angew. Chem. Int. Ed.* **63**, e202405950 (2024).
12. Zhang, S.-K. et al. Interfacial electrochemical-chemical reaction coupling for efficient olefin oxidation to glycols. *Joule* **7**, 1887–1901 (2023).
13. Ghannadzadeh, A. & Tarighaleslami, A. H. Exergy-aided environmental life cycle assessment of propylene oxide production. *Int. J. Life Cycle Assess.* **27**, 20–37 (2021).
14. Wang, J. et al. Spatial-coupled Ampere-level electrochemical propylene epoxidation over RuO_2/Ti hollow-fiber penetration electrodes. *Angew. Chem. Int. Ed.* **63**, e202411173 (2024).
15. Wang, M. et al. *Greenhouse Gases, Regulated Emissions, and Energy Use in Technologies Model (2023.Net)* (US DOE Office of Energy Efficiency and Renewable Energy (EERE), 2023); https://www.osti.gov/doecode/biblio/113174
16. Lin, Y. et al. V activated electro-epoxidation catalyst in membrane electrode assembly system for the production of propylene oxide. *Nat. Commun.* **16**, 3113 (2025).
17. Dong, H. et al. Electrochemical epoxidation enhanced by C_2H_4 activation and hydroxyl generation at the Ag/SnO_2 interface. *Nat. Commun.* **16**, 1901 (2025).
18. Ke, J. et al. Dynamically reversible interconversion of molecular catalysts for efficient electrooxidation of propylene into propylene glycol. *J. Am. Chem. Soc.* **145**, 9104–9111 (2023).
19. Li, A.-Z. et al. One-step electrochemical ethylene-to-ethylene glycol conversion over a multitasking molecular catalyst. *J. Am. Chem. Soc.* **146**, 5622–5633 (2024).
20. Chung, M. et al. Direct propylene epoxidation via water activation over Pd-Pt electrocatalysts. *Science* **383**, 49–55 (2024).
21. Lum, Y. et al. Tuning OH binding energy enables selective electrochemical oxidation of ethylene to ethylene glycol. *Nat. Catal.* **3**, 14–22 (2020).
22. Huang, J. E. et al. Selective electrified propylene-to-propylene glycol oxidation on activated Rh-doped Pd. *J. Am. Chem. Soc.* **146**, 8641–8649 (2024).
23. Dorchies, F. et al. Controlling the hydrophilicity of the electrochemical interface to modulate the oxygen-atom transfer in electrocatalytic epoxidation reactions. *J. Am. Chem. Soc.* **144**, 22734–22746 (2022).
24. Wang, X. et al. Ligand tuning of molecular Ag catalysts enables efficient direct propylene electrooxidation to propylene glycol. *J. Am. Chem. Soc.* **147**, 23090–23102 (2025).
25. Chen, W. et al. Vacancy-induced catalytic mechanism for alcohol electrooxidation on nickel-based electrocatalyst. *Angew. Chem. Int. Ed.* **63**, e202316449 (2024).
26. Oener, S. Z., Bergmann, A. & Cuenya, B. R. Designing active oxides for a durable oxygen evolution reaction. *Nat. Synth.* **2**, 817–827 (2023).
27. Zhang, J. et al. Tantalum-stabilized ruthenium oxide electrocatalysts for industrial water electrolysis. *Science* **387**, 48–55 (2025).
28. Liu, X.-C. et al. Reaction mechanism and selectivity tuning of propene oxidation at the electrochemical interface. *J. Am. Chem. Soc.* **144**, 20895–20902 (2022).
29. Ghosh, R., Hopping, G. M., Lu, J. W., Hollyfield, D. W. & Flaherty, D. W. Alkene epoxidation and oxygen evolution reactions compete for reactive surface oxygen atoms on gold anodes. *J. Am. Chem. Soc.* **147**, 1482–1496 (2025).
30. Li, H., Abraham, C. S., Anand, M., Cao, A. & Nørskov, J. K. Opportunities and challenges in electrolytic propylene epoxidation. *J. Phys. Chem. Lett.* **13**, 2057–2063 (2022).
31. Yun, T. G. et al. Extrinsic and intrinsic factors governing the electrochemical oxidation of propylene in aqueous solutions. *J. Am. Chem. Soc.* **147**, 12318–12330 (2025).
32. Winiwarter, A. et al. Towards an atomistic understanding of electrocatalytic partial hydrocarbon oxidation: propene on palladium. *Energy Environ. Sci.* **12**, 1055–1067 (2019).
33. Ran, P. et al. Universal high-efficiency electrocatalytic olefin epoxidation via a surface-confined radical promotion. *Nat. Commun.* **15**, 8877 (2024).
34. Silvioli, L. et al. Rational catalyst design for higher propene partial electro-oxidation activity by alloying Pd with Au. *J. Phys. Chem. C* **126**, 14487–14499 (2022).
35. Liang, C. et al. Role of electrolyte pH on water oxidation for iridium oxides. *J. Am. Chem. Soc.* **146**, 8928–8938 (2024).
36. Shi, Y. et al. Dual cocatalytic sites synergize NiFe layered double hydroxide to boost oxygen evolution reaction in anion exchange membrane water electrolyzer. *Adv. Energy Mater.* **14**, 2402046 (2024).
37. Zhang, A., Liang, Y., Zhang, H., Geng, Z. & Zeng, J. Doping regulation in transition metal compounds for electrocatalysis. *Chem. Soc. Rev.* **50**, 9817–9844 (2021).
38. Gao, W. et al. Determining the adsorption energies of small molecules with the intrinsic properties of adsorbates and substrates. *Nat. Commun.* **11**, 1196 (2020).
39. Argus Media. *Argus Propylene Oxide and Derivatives* https://www.argusmedia.com/en/solutions/products/argus-propylene-oxide-and-derivatives (2024).

40. Wang, Y.-H. et al. In situ Raman spectroscopy reveals the structure and dissociation of interfacial water. *Nature* **600**, 81–85 (2021).
41. Sugimura, F. et al. In situ observation of Pt oxides on the low index planes of Pt using surface enhanced Raman spectroscopy. *Phys. Chem. Chem. Phys.* **19**, 27570–27579 (2017).
42. Sum, O. S. N. et al. Raman investigation of the O_2, Pt/YSZ electrode under polarization. *Solid State Ionics* **176**, 2599–2607 (2005).
43. Qian, Z.-X. et al. Direct capturing and regulating key intermediates for high-efficiency oxygen evolution reactions. *Small Methods* **8**, 2301504 (2024).
44. Eads, C. N. et al. Resolving active species during the carbon monoxide oxidation over Pt(111) on the microsecond timescale. *Nat. Commun.* **16**, 1216 (2025).
45. Winiwarter, A. et al. CO as a probe molecule to study surface adsorbates during electrochemical oxidation of propene. *ChemElectroChem* **8**, 250–256 (2021).
46. Dent, A. L. & Kokes, R. J. The nature of adsorbed propylene on zinc oxide. *J. Am. Chem. Soc.* **92**, 6709–6718 (1970).
47. Liu, B. et al. Ligand-free noble metal nanocluster catalysts on carbon supports via 'soft' nitriding. *J. Am. Chem. Soc.* **138**, 4718–4721 (2016).
48. Xu, G.-Y. et al. Metal-support interactions alter the active species on IrOx for electrocatalytic water oxidation. *J. Mater. Chem. A* **11**, 15204–15210 (2023).
49. Kresse, G. & Joubert, D. From ultrasoft pseudopotentials to the projector augmented-wave method. *Phys. Rev. B* **59**, 1758–1775 (1999).
50. Kresse, G. & Furthmüller, J. Efficient iterative schemes for *ab initio* total-energy calculations using a plane-wave basis set. *Phys. Rev. B* **54**, 11169–11186 (1996).
51. Blöchl, P. E. Projector augmented-wave method. *Phys. Rev. B* **50**, 17953–17979 (1994).
52. Perdew, J. P., Burke, K. & Ernzerhof, M. Generalized gradient approximation made simple. *Phys. Rev. Lett.* **77**, 3865–3868 (1996).
53. Perdew, J. P. et al. Atoms, molecules, solids, and surfaces: Applications of the generalized gradient approximation for exchange and correlation. *Phys. Rev. B* **46**, 6671–6687 (1992).
54. Grimme, S., Antony, J., Ehrlich, S. & Krieg, H. A consistent and accurate *ab initio* parametrization of density functional dispersion correction (DFT-D) for the 94 elements H-Pu. *J. Chem. Phys.* **132**, 154104 (2010).
55. Grimme, S., Ehrlich, S. & Goerigk, L. Effect of the damping function in dispersion corrected density functional theory. *J. Comput. Chem.* **32**, 1456–1465 (2011).
56. Mathew, K., Kolluru, V. S. C., Mula, S., Steinmann, S. N. & Hennig, R. G. Implicit self-consistent electrolyte model in plane-wave density-functional theory. *J. Chem. Phys.* **151**, 234101 (2019).
57. Mathew, K., Sundararaman, R., Letchworth-Weaver, K., Arias, T. A. & Hennig, R. G. Implicit solvation model for density-functional study of nanocrystal surfaces and reaction pathways. *J. Chem. Phys.* **140**, 084106 (2014).

Acknowledgements

The XAS research was undertaken on the XAS beamline (23013 and 23014) at the Australian Synchrotron, part of ANSTO. We acknowledge the facilities and the scientific and technical support provided by Sydney Analytical, a core research facility at The University of Sydney.

Author contributions

E.H.S. and K.X. supervised the project. Y.L. synthesized the catalysts and performed all electrochemical experiments. Y.C. conducted the DFT calculations. Y.Y. and F.L. conducted the operando ATR-SEIRAS and XAS measurements. R.X. carried out the techno-economic analysis. Z.Z. assisted with XAS data processing and fitting. J.E.H. contributed to MEA testing. B.P. and Z.L. performed the electron microscopy characterization. H.Z. assisted with operando Raman measurements and spectral analysis. A.H.S. analysed the electrochemical stripping data. Y.J. conducted the XRD measurements. Y.L., E.H.S. and K.X. co-wrote the manuscript with input from all co-authors. All authors discussed the results and contributed to the final manuscript preparation.

Funding

E.H.S. and K.X. acknowledge funding from Braskem America, Inc. F.L. acknowledges the ARC Centre of Excellence for Green Electrochemical Transformation of Carbon Dioxide (CE230100017), funded by the Australian government.

Competing interests

Y.L., E.H.S. and K.X. are inventors on a patent disclosure entitled 'Efficient Propylene Electro-Epoxidation to Pure Propylene Oxide Using Indium-Doped PtPd Oxide Catalysts' filed with the Northwestern University Innovation and New Venture Office. The other authors declare no competing interests.

Additional information

Supplementary information The online version contains supplementary material available at https://doi.org/10.1038/s44160-026-01104-6.

Correspondence and requests for materials should be addressed to Ke Xie or Edward H. Sargent.

Peer review information *Nature Synthesis* thanks Chuncheng Chen, Zhongtao Li and the other, anonymous, reviewer(s) for their contribution to the peer review of this work. Primary Handling Editor: Jet-Sing Lee, in collaboration with the *Nature Synthesis* team.